Showcasing research from Professor Albert Tarancón's laboratory, Catalonia Institute for Energy Research (IREC), Catalonia, Spain.
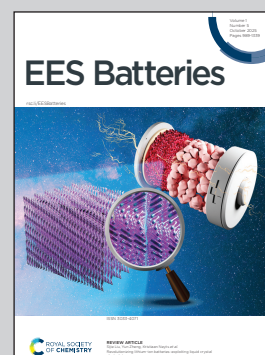
Unraveling nanoscale interfacial kinetics in battery cathodes through *operando* tip-enhanced Raman spectroscopy

Shining a nano-spotlight on working cathodes, operando TERS captures interfacial kinetics with chemical specificity. The approach resolves grain versus boundary behavior, visualizes phase fronts, and quantifies lithium transport as it happens. These insights expose hidden rate limitations and provide a blueprint for tailoring interfaces in next-generation batteries.

Image designed and illustrated by Princess Romero (IREC).

Image reproduced by permission of Juan Carlos Gonzalez-Rosillo, Alex Morata and Albert Tarancón.

ROYAL SOCIETY OF CHEMISTRY

rsc.li/EESBatteries

EES Batteries

Check for updates

Unraveling nanoscale interfacial kinetics in battery cathodes through *operando* tip-enhanced Raman spectroscopy†

Beatrice Laurenti, ‡[a] Juan Carlos Gonzalez-Rosillo, *‡[a] Francesco Chiabrera, [a] Alice Fiocco,[b] Fernanda Monteiro Freitas, [a] Marc Chaigneau, [b] Alex Morata *[a] and Albert Tarancón *[a,c]

Understanding interfacial phenomena at the micro- and nanoscale is essential for improving the performance of energy storage technologies such as lithium-ion batteries. However, probing the chemical and structural evolution of buried interfaces during operation remains a major experimental challenge. Here, we present the first implementation of *operando* Tip-Enhanced Raman Spectroscopy (TERS) to track nanoscale lithium-ion dynamics in working battery electrodes. Using $LiMn_2O_4$ and $LiFePO_4$ thin films as model systems, we demonstrate that TERS can determine grain- and grain-boundary-specific behavior with spatial and temporal resolution. In $LiMn_2O_4$, we observe a delayed appearance of the λ-MnO_2 phase at grain boundaries during delithiation, which is consistent with faster Li^+ diffusion in these regions and is supported in this work by 2D finite-element simulations. In contrast, $LiFePO_4$ exhibits reduced spectral visibility under *operando* conditions, yet systematic background modulation enables tracking of surface-level redox processes. These results establish *operando* TERS as a powerful technique for probing local ionic transport and interfacial chemistry in complex energy materials, with broad implications for the design and optimization of next-generation battery systems.

Broader context

The global transition towards renewable energy sources and electrified transportation heavily relies on high-performance energy storage solutions, especially batteries. However, many promising battery technologies face fundamental limitations associated with interfacial phenomena occurring at extremely small length scales, which significantly affect overall battery efficiency, lifetime, and safety. These interfaces, such as grain boundaries and electrode–electrolyte interfaces, can either facilitate or hinder ion transport, making their detailed understanding crucial for optimizing battery performance. Despite advancements, conventional techniques used to study these phenomena generally provide averaged information and lack sufficient spatial resolution, limiting our ability to design better-performing, longer-lasting, and safer batteries. The development of *operando* Tip-Enhanced Raman Spectroscopy (TERS), as demonstrated in this study, addresses this critical gap by enabling direct visualization of chemical and structural changes at nanoscale interfaces under realistic operating conditions.

Introduction

A battery consists of numerous interfaces, each playing a distinct and often dominant role in its overall performance, efficiency, and longevity. These interfacial interactions govern essential processes, such as ion transport, charge transfer, and chemical stability. Many studies have emphasized that interface design, particularly grain boundaries, is a crucial factor controlling both ionic and electronic transport.[1–4] Since these nanometric-length scale interfaces undergo dynamic chemical and structural changes during operation, it is imperative to develop advanced characterization techniques with sufficient resolution and sensitivity capable of capturing the real-time chemical evolution of critical interfaces.

One of the most widely used techniques for understanding the complex interplay of interfaces involved in electrochemical responses is Electrochemical Impedance Spectroscopy (EIS). EIS is widely used for decoupling phenomena at different time

*[a]Nanoionics and Fuel Cells, Catalonia Institute for Energy Research (IREC), Jardins de les Dones de Negre 1, 08930 Sant Adrià del Besòs, Barcelona, Spain.
E-mail: jcgonzalez@irec.cat, amorata@irec.cat, atarancon@irec.cat*
[b]HORIBA France SAS, 14 bd Thomas Gobert, 91120 Palaiseau, France
[c]Catalan Institution for Research and Advanced Studies (ICREA), Passeig Lluís Companys 23, 08010 Barcelona, Spain
†Electronic supplementary information (ESI) available. See DOI: https://doi.org/10.1039/d5eb00094g
‡Shared first co-authorship.

scales, which is of major importance for understanding ionic conduction, charge transfer mechanisms or diffusion-limited processes.[5,6] However, EIS lacks the spatial resolution needed to directly visualize local heterogeneities, such as grain boundaries, offering instead an averaged response. To achieve higher spatial resolution, techniques such as Scanning Ion Conductance Microscopy (SICM) and Scanning Electrochemical Cell Microscopy (SECCM) have been developed. SICM measures localized ionic currents rather than electrochemical redox processes, while SECCM provides localized redox information but typically at lower spatial resolution (~100 nm) compared to SICM.[4,7–9] Both techniques, however, remain inherently confined to the nanoscale region beneath the nanopipette tip acting as the active electrode, limiting their effectiveness in probing very narrow interfaces. Electrochemical Strain Microscopy (ESM), with its superior spatial resolution (~10 nm, limited mainly by tip geometry), uses a biased AFM tip to induce localized ionic transport and detects the resulting mechanical deformation due to ion migration.[10–12] Despite its high resolution, ESM only indirectly probes electrochemical phenomena, and its signals are strongly influenced by mechanical coupling between the tip and sample. Furthermore, SICM, SECCM, and ESM can introduce high local electric fields and potential cross-talk between topographical and electrochemical signals, complicating the interpretation of electrochemical behavior, particularly in operando studies of structurally complex regions such as grain boundaries.

Over the past decades, significant advances have been made in the 2D and 3D analysis of grain boundaries. Advanced techniques such Atom Probe Tomography (APT) and High-Resolution Transmission Electron Microscopy (HRTEM) enable nanoscale characterization of grain boundaries.[13] HRTEM provides high-resolution 2D images that reveal the atomic structure of materials, allowing direct visualization of grain boundary structures, defect distributions, and grain orientation with atomic-level precision.[14] When coupled with Electron Energy Loss Spectroscopy (EELS) or Energy Dispersive X-ray Spectroscopy (EDS), HRTEM can provide additional compositional information.[15] APT offers 3D images containing information of individual detected atomic species with sub-nanometer spatial resolution and extremely high analytical sensitivity.[16,17] Very recently, our group demonstrated how APT can provide a 3D-resolved reconstruction with isotopic sensitivity,[18] directly observing oxygen diffusion pathways at grain boundaries.[19] However, these techniques require specific sample geometries, and the preparation process can be notably challenging and time-consuming and costly. These challenges highlight the need for more practical approaches, especially for operando studies.

A powerful tool for nanoscale chemical characterization that has emerged over the past two decades, is Scanning Probe Microscopy – Tip-Enhanced Raman Spectroscopy (SPM-TERS).[20–23] This technique combines a Scanning Probe Microscope (SPM) and Raman Spectroscopy, taking advantage of Scanning Tunneling Microscopes (STM) or Atomic Force

Microscopes (AFM). These TERS approaches offer nanometric resolution and high-sensitivity spectroscopy and imaging, enabling the acquisition of local chemical information. By focusing a laser onto a sharp metal (or metal-coated) SPM tip, it is possible to amplify the electromagnetic field – and thus the Raman signal – through a combination of localized surface plasmon resonance (LSP)[24] and the lighting rod effect.[25,26] This enhancement is confined to the vicinity of the SPM tip, enabling nanoscale resolution, limited by the probe itself. Our group recently studied $LiMn_2O_4$ thin film using AFM-based TERS, demonstrating the technique's sensitivity to surface defects and grain boundary chemistry.[27] TERS offers significant benefits in terms of time efficiency and reduced complexity compared to the aforementioned techniques. In addition, TERS does not require any complex sample preparation, can be used in gas and temperature-controlled conditions and does not require long data acquisition times, enabling its use to monitor a variety of electrochemical processes, also in operando. Unlike ESM, SICM, or SECCM, operando TERS measurements offer the critical advantage that the entire sample can be electrochemically cycled rather than just the localized area directly beneath the tip, enabling more representative and accurate operando studies.

Despite the extensive scientific literature on batteries, relatively few studies have explored the potential of TERS in this context. This is likely due to challenges associated with performing "non-gap mode"[28] measurements on rough or thick materials and achieving a strong TERS signal from bulk samples or thick films grown on non-transparent or metallic substrates. In gap mode, strong field enhancement arises from the confined electromagnetic field generated between a metallic tip and a metallic substrate, as opposed to non-gap mode configurations, which operate on non-metallic or irregular surfaces and rely solely on the tip for enhancement.[29] The surface sensitivity of TERS makes it uniquely suited for detecting cathode–electrolyte interphase (CEI) or solid–electrolyte interphase (SEI) layers, providing spatially resolved insights into interfacial degradation processes. For that, among the limited studies available, the pioneering work of Nanda et al.[30,31] on SEI composition in silicon thin film anodes and Dinda et al.[32] study on both SEI and CEI in sodium batteries stand out. In the same direction, we recently reported the first ex situ studies of $LiMn_2O_4$ thin films cycled in aqueous electrolyte, revealing the presence of Mn_3O_4 and sulfate adsorbates at grain boundaries that evolve with cycling.[28] However, to the best of our knowledge, no studies have reported the implementation of operando TERS in batteries.

Herein, we present the implementation of operando TERS, integrated into an atomic force microscope and coupled to a custom-designed electrochemical cell, to probe lithium-ion dynamics at the grain and grain boundary level in working battery materials. We focus primarily on $LiMn_2O_4$ thin films, a model system where grain boundaries are believed to promote fast Li^+ transport.[33–35] By positioning the TERS tip with nanometric precision on top of individual grains or at

grain boundaries during cyclic voltammetry, we capture time-resolved vibrational signatures that reflect local lithiation and delithiation processes. Our experiments reveal a clear delay in the emergence of the λ-MnO$_2$ phase at grain boundaries, consistent with faster Li$^+$ diffusion compared to the grain interior. These findings are supported by two-dimensional finite-element simulations, confirming the ability of TERS to resolve interface-specific transport kinetics *operando*. To test the broader applicability of this method, we also investigate LiFePO$_4$ thin films under similar conditions. Although *operando* spectral resolution is limited in this case, systematic background modulation remains detectable and correlated with the electrochemical state, demonstrating the sensitivity of TERS even under spectroscopically challenging environments. Together, these results establish *operando* TERS as a powerful platform for probing nanoscale ion transport and interfacial reactivity in complex electrochemical systems.

Results and discussion

Operando TERS in LiMn$_2$O$_4$

Building on our previous success in employing TERS to characterize LiMn$_2$O$_4$ thin films under *ex situ* conditions,[28] we implemented a custom electrochemical cell to enable *operando* TERS measurements. This setup was integrated into a commercial AFM system from Horiba, allowing real-time monitoring of structural and compositional changes in LiMn$_2$O$_4$ as the entire film undergoes electrochemical cycling with the tip acting as a local nano-Raman probe. Further details on the cell design and experimental configuration are provided in the Methods section and the ESI (section I).†

To establish the viability of TERS under liquid electrochemical conditions, we first evaluated signal enhancement in a LiMn$_2$O$_4$ thin film immersed in aqueous electrolyte. As shown in Fig. 1a, Raman spectra acquired with the tip in contact (TERS mode) exhibit an overall signal intensity ampli-
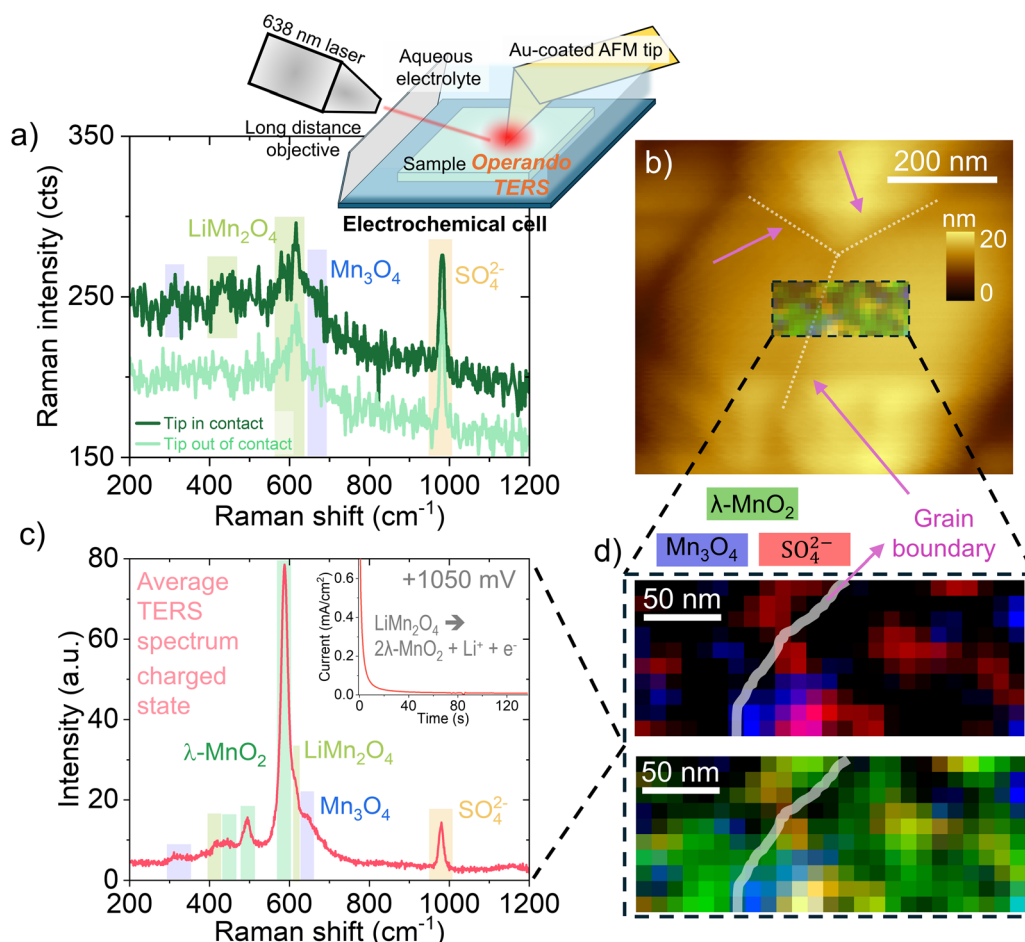

Fig. 1 (a) Comparison of Raman signal of far-field (tip out of contact, in light green) and near-field (tip in contact, TERS mode, in dark green) modes. Inset: sketch of the measurement setup for *operando* TERS. (b) AFM topography map (600 × 600 nm^2) with the TERS map overlaid at the precise region where it was measured. Spatial resolution was set to 10 nm per pixel, 1 s per pixel acquisition time. (c) Average TERS spectrum from the TERS map after applying a constant voltage step at 1050 mV, for inducing the discharge process (delithiation). Band assignment is discussed in the text and shadowed with different colors for each phase. (d) TERS map showing the relative intensities of different bands (green – λ-MnO$_2$, blue – Mn$_3$O$_4$ and red – sulfate ions). Top map shows the overlay of blue and red, while bottom map shows the overlay of blue, red and green.

fication of approximately 25% compared to spectra collected with the tip out of contact (oscillating at ~20 nm amplitude). Several Raman modes are observed and assigned based on previous literature:[28,36,37] the dominant peaks (bands at ~420 and 620 cm^{-1}) correspond to $LiMn_2O_4$, while additional features are attributed to trace Mn_3O_4 (bands at ~310 and 660 cm^{-1}) impurities and a band near ~980 cm^{-1} originating from sulfate ions in the aqueous electrolyte. This spectral fingerprint confirms that TERS enhancement persists in liquid environments and improves spectral resolution for weaker vibrational modes, in line with our previous *ex situ* studies on $LiMn_2O_4$ thin films. In particular, vibrational bands in the 200–400 cm^{-1} region become more prominent under TERS conditions, indicating enhanced sensitivity to lattice modes of the $LiMn_2O_4$ and Mn_3O_4 phases.

We next acquired an AFM topography image over a 600 × 600 nm^2 region containing several grains (Fig. 1b), from which a 250 × 100 nm^2 area was selected between two grains for spatially resolved TERS mapping. This quasi-*operando* experiment was conducted in the charged state after applying a constant potential of +1050 mV, as shown in the inset of Fig. 1c, ensuring surface transformation prior to spectral acquisition,[38] according to the expected electrochemical reaction:

$$LiMn_2O_4 \rightarrow 2\lambda - MnO_2 + Li^+ + e^- \quad (1)$$
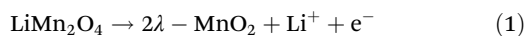
Averaging the collected spectra across the whole region yields the spectrum in Fig. 1c, where bands at ~498 and ~588 cm^{-1} are consistent with the formation of λ-MnO_2, the fully delithiated phase. Notably, the Raman signal from λ-MnO_2 is strongly enhanced compared to $LiMn_2O_4$, a well-known effect also observed at the macro-scale due to the resonance of the λ-MnO_2 phase with the excitation laser.[39] Residual features from $LiMn_2O_4$ and Mn_3O_4 are also present, along with the sulfate band from the electrolyte, in agreement with our previous *ex situ* studies.[28] Following the methodology established in our earlier work, we constructed TERS intensity maps by tracking the spatial variation of selected vibrational modes (Fig. 1d). A white transparent line marks the approximate position of the grain boundary as inferred from the AFM topography. The maps reveal that Mn_3O_4 and sulfate signals are locally enhanced at the grain boundary, while the λ-MnO_2 phase dominates the overall spectral response. These results are in line with our previous *ex situ* observations and confirm that TERS enables nanometric spatial resolution of electrochemical phase evolution. Having demonstrated the chemical sensitivity and spatial resolution of TERS under quasi-*operando* conditions, we then performed fully *operando* measurements during electrochemical cycling. We selected a well-defined grain from the same AFM topography map (Fig. 2a) and positioned the tip on top of a grain, far from the grain boundary. Cyclic voltammetry (CV) was performed while simultaneously acquiring time-resolved TERS spectra at a fixed point. The acquisition parameters (1.7 seconds per spectrum) were optimized to capture spectral changes with sufficient temporal resolution (see Methods for details). CV was used to

drive lithium extraction (delithiation) and insertion (lithiation) in the $LiMn_2O_4$ film. During charge, the voltammogram displays two characteristic redox peaks: the first corresponds to the formation of a partially delithiated $Li_{0.5}Mn_2O_4$ intermediate, while the second is associated with further delithiation toward the λ-MnO_2 phase. These structural transitions are reversible upon discharge.

Fig. 2a displays the changes of the Raman intensity over time, overlaid with the CV current profile using a common time axis. Notably, the Raman intensity around 590 cm^{-1}, associated with the λ-MnO_2 phase, increases in parallel with the positive current peak in the CV. This clearly demonstrates the ability of *operando* TERS to track phase transitions with nanoscale resolution, even at relatively fast scan rates of 5 mV s^{-1}. To further illustrate the phase change, we compare two spectra from the TERS time series: one acquired at $t = 10$ s (before full delithiation), and another at $t = 50$ s (after delithiation). As shown in Fig. 2c, the λ-MnO_2 spectral signature appears only after oxidation, confirming the formation of the delithiated phase following lithium extraction from $LiMn_2O_4$. Meanwhile, the prominent peak at ~980 cm^{-1}, assigned to the sulfate ion (SO_4^{2-}) from the dissociation of the Li_2SO_4 electrolyte,[27] remains unchanged throughout the CV. Note that the apparent difference in sulfate peak intensity between the two spectra in Fig. 2c is due to the different vertical scales used for plotting.

We next repeated this procedure, positioning the tip and laser on a grain boundary (white cross in the topography image, inset of Fig. 2b). As shown in Fig. 2b, the intensity of the λ-MnO_2 peak again increases at the second delithiation peak in the CV. A closer examination of the high-intensity region in the time map (red zone) reveals a consistent shift in the onset of the phase transition, suggesting a delayed response at the grain boundary compared to the grain interior. To quantify this difference, we extracted the average Raman intensity in the 580–596 cm^{-1} range (corresponding to λ-MnO_2 phase) for both the grain and grain boundary measurements and plotted them alongside the corresponding CV scans (Fig. 3d and e, respectively). Analysis of the λ-MnO_2 peak intensity reveals a measurable delay of approximately 6 seconds in the emergence of the delithiated phase at the grain boundary. This observed delay suggests that lithium is extracted more efficiently from the grain boundary, resulting in slower local accumulation of delithiated products, which is a signature of higher Li-ion diffusivity.

In light of these observations, we propose that the delayed appearance of the λ-MnO_2 phase at grain boundaries reflects a higher Li-ion diffusivity in these regions, which translates into faster deintercalation kinetics. Although this is the first time such behavior is observed *via operando* TERS, multiple studies have reported up to four orders of magnitude faster lithium diffusion along grain boundaries,[33–35] often attributed to the presence of negatively charged lithium vacancies around the grain boundary core.[35] Indeed, in our previous works we identified vacancy clusters of negatively charged vacancies accumulating at grain boundaries *via* Positron Annihilation
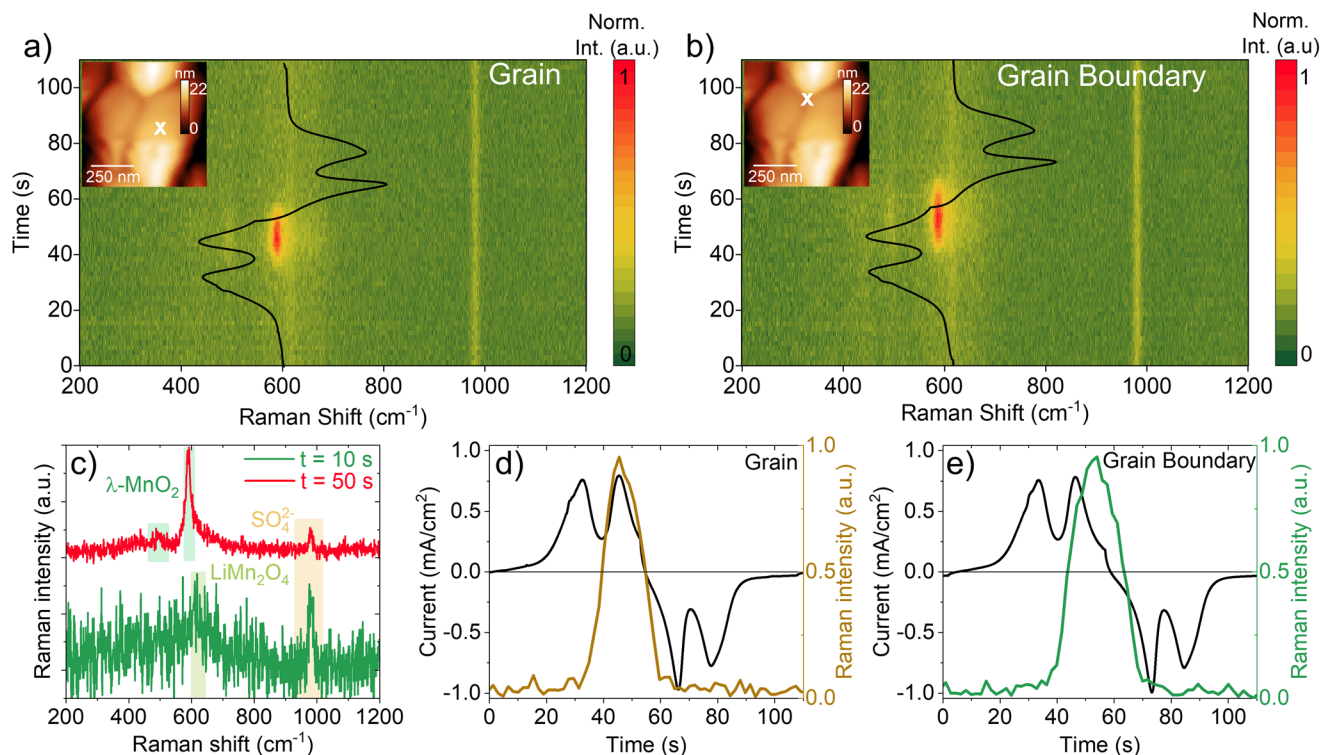
Fig. 2 TERS time map overlaid with the current density for grain (a) and grain boundary (b) with the inset showing the AFM topography with the tip position indicated with white crosses. (c) Raman spectra extracted at t = 10 s (green) and t = 50 s (red) from the TERS time maps of the grain. The two spectra are plotted using separate vertical axes for clarity: the red spectrum (left axis) spans from −1.1 to 0.8, while the green spectrum (right axis) spans from −0.05 to 0.4. No multiplication or artificial scaling was applied; both spectra belong to the same normalized data set. (d) and (e) Averaged TERS intensity (580–596 cm^{-1}) with overlaid current density of the cyclic voltammetry for grain (d) and grain boundary (e). Note that these graphs correspond to the second cycle of a set of 3 consecutive scans, with time normalized for ease of visualization, see section II in the ESI.†

Lifetime Spectroscopy.[27,40] These defects typically surround the positively charged grain boundary core,[34,41,42] balancing the electrostatic interactions and forming a space charge layer.[34] Although space-charge layers are typically considered detrimental to Li-ion transport in most Li-based materials,[43,44] LiMn$_2$O$_4$ appears to be an exception: here, ionic transport is significantly enhanced at grain boundaries. Remarkably, this effect is sufficiently pronounced and spatially extended to be detected by *operando* TERS, even with our spatial resolution limited by a ~20 nm commercial tip radius.[41]

It is worth noting that the slightly longer persistence of the λ-MnO$_2$ signal at the grain boundary may be influenced by subtle differences in the current level at the turning point of the voltage sweep (1.05 V) that arise from cycle to cycle. This current level is also different between the experimental and the simulated, as seen in Fig. 3a. However, this factor alone cannot account for the delayed onset of the phase transition, as measurements at both grain and grain boundary locations were independently repeated three times, consistently showing the same behavior. Post-mortem *ex situ* TERS analysis reveals early sulfate adsorption and preferential presence of Mn$_3$O$_4$ at grain boundaries, with stronger contrast than observed in conventional Raman (see ESI, section II†).

To support our experimental findings, we performed two-dimensional Finite Element Method (FEM) simulations that replicate an equivalent electrochemical experiment. The model describes electrochemical Li intercalation and diffusion in a layer with grain boundary diffusivity four order of magnitudes higher than the bulk one (see Methods for details). As a first step, we simulated a CV curve to verify that the model accurately reproduces the overall electrochemical response of the film (Fig. 3a), obtaining close agreement between the simulated and experimental CVs. The extracted values of bulk chemical diffusivity (10^{-11} cm^2 s^{-1}) and charge transfer resistance (0.6 Ω cm^2) are comparable with literature values, endorsing the model.[45-47] Discrepancies between model and experiments are mainly due to differences in the equilibrium voltage profiles, which were directly assumed from literature,[46] and are not expected to influence the main conclusions of the simulations. We then used the model to track the Li$^+$ concentration as a function of time (Fig. 3c) and spatial position across the film, extracting concentration maps representing the grain bulk and at the grain boundary, following the schematic shown in Fig. 3b. The concentration maps (Fig. 3d, snapshots at t = 35 s, 50 s, and 65 s) reveal the time evolution of the Li$^+$ distribution. At the onset of lithium deintercalation, Li$^+$ concentration remains higher at the grain boundaries, particularly near the subsurface, compared to the grain interior, consistent with the delayed phase transition observed *via operando* TERS. Conversely, during reintercalation (t ≈ 65 s), the
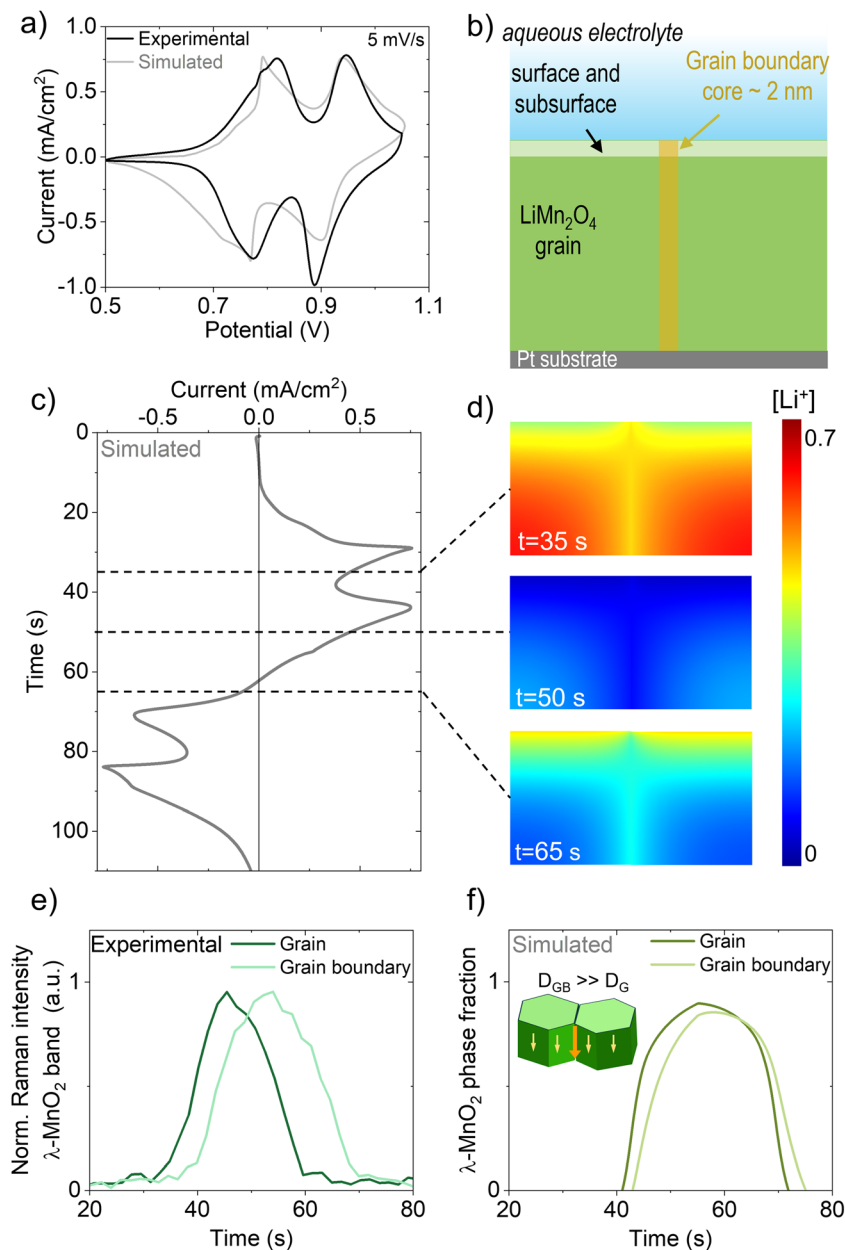
Fig. 3 2D-FEM simulations: (a) comparison between experimental (black) and simulated (grey) CVs; (b) sketch of grain and grain boundary simulated section; (c) simulated current profile during time; (d) dynamics visualization of Li$^+$ concentration across the film, starting from the top: image capture at $t = 35$ s, $t = 50$ s and $t = 65$. (e) Intensity averaged over the $580-596$ cm^{-1} region *versus* time for grain and grain boundary. (f) Simulations of the λ-MnO$_2$ phase fraction for the case where fast Li$^+$ diffusion at the grain boundaries is assumed.

Li$^+$ front advances inward from the subsurface, while the grain boundaries exhibit relatively lower concentrations. To directly compare our time-resolved TERS measurements with the simulations, we set Li ≤ 0.4 in Li$_x$Mn$_2$O$_4$ as the threshold for the phase transition into λ-MnO$_2$,[41] focusing on a 20 nm subsurface region to approximate the TERS sensitivity at both the grain center and the grain boundary. The resulting simulated profiles (Fig. 3f) reproduce the experimental delay observed between the grain and grain boundary regions (Fig. 3e) for both deintercalation and reintercalation processes. This agree-

ment is achieved by incorporating a single assumption, well supported by literature, that lithium diffusion is faster at grain boundaries. Additional simulations investigating alternative explanations, such as local shifts in insertion potential or variations in charge transfer resistance, revealed negligible contributions to the observed delays (see ESI, section II†). To assist in visualizing this mechanism, a supplementary video (Video S1†) is provided, showing the time evolution of Li-ion concentration and simulated Raman response at both grain and grain boundary locations.

While our FEM model successfully captures the kinetic delay of lithium deintercalation between grain and grain boundary regions, a notable deviation remains: all simulated profiles peak around the maximum applied potential, whereas the Raman signal from *operando* TERS reaches its maximum earlier, during the rising portion of the voltage sweep (see ESI, section II†). This consistent discrepancy, observed both at grains and grain boundaries, cannot be explained by bulk transport dynamics alone. We propose that this behavior originates from surface-specific processes not captured in our model, revealing one of the most exciting strengths of *operando* TERS: its ability to selectively probe interfacial charge dynamics with nanometric resolution in realistic electrochemical environments.

Recent works have highlighted that surface-limited or interfacial processes can significantly influence the overall battery response. Halldin Stenlid *et al.*[48] presented a state-of-the-art CIET (Coupled Ion-Electron Transfer) framework that combines constrained and constant potential DFT to predict charge transfer kinetics at the interface, explicitly incorporating solvent coordination and ion adsorption structures. Their results demonstrate that interfacial ion and electron transfer can dominate the local reaction landscape. While our model focuses solely on bulk diffusion, the TERS signal can still capture this interfacial complexity. Moreover, we add an additional layer of spatial resolution by specifically interrogating grain boundaries, which are interfaces that, despite their known influence on ionic transport, remain largely uncharacterized under *operando* conditions. The potential impact is particularly pronounced for small-grained materials, where the density of grain boundaries can directly shape device performance.

From a different angle, the work of Xiao *et al.*[49] illustrates how space charge layers can give rise to interfacial lithium storage in mixed conductors, showing capacitive-like behavior localized at solid–solid interfaces. The early appearance of λ-MnO$_2$ signatures in our TERS data may represent a related phenomenon, *i.e.*, lithium depletion at the surface induced by space charge effects that could be studied as a function of the state-of-charge *in operando* conditions. Thickness-dependent studies will be performed for that, together with further defect-chemical modeling. Additionally, Huang *et al.*[50] recently demonstrated that spontaneous H$_3$O$^+$ intercalation into the LiMn$_2$O$_4$ lattice during cycling in aqueous electrolytes can dramatically alter local redox behavior and structure by forming Mn^{4+}-rich surface layers. Although our samples were not subjected to prolonged cycling to avoid such cumulative changes, these phenomena deserve focused investigation in future work.

Overall, despite the simplicity of our FEM model, which excludes surface and electrolyte-specific effects, its ability to reproduce key experimental trends highlights the robustness of the mechanistic picture proposed. Yet, the deviation in the timing of the phase transition peak is not a minor artifact, but rather a revealing clue: it points toward electrochemical complexity at the nanoscale that demands spatially and chemically resolved *operando* techniques. *Operando* TERS has proven capable of capturing these subtle but critical effects, often not visible by more conventional methods.

Extending *operando* TERS to LiFePO$_4$

Having established the sensitivity and spatial selectivity of this technique in LiMn$_2$O$_4$, we now extend our *operando* TERS methodology to LiFePO$_4$ thin films, a second model system with fundamentally different phase transformation mechanisms and transport properties. This comparison enables us to further test the universality and limits of nanoscale *operando* Raman as a probe of local redox dynamics under working conditions. Prior to *operando* measurements, we characterized LiFePO$_4$ thin films *via ex situ* TERS and conventional Raman spectroscopy to establish a reference (see ESI, section III†). As shown in Fig. 4a, both techniques detect mainly the LiFePO$_4$ modes (at ~948 cm^{-1} the main mode, and minor modes at ~430, 483, 570, 628, 990 and 1070 cm^{-1}),[12,16,22] but only TERS reveals an additional broad feature near 750 cm^{-1}, attributed to a superficial Fe$_3$O$_4$ phase. This secondary signal, mapped across the film surface (Fig. 4b and c), highlights the enhanced surface sensitivity of TERS, revealing the presence of small regions in the map rich in Fe$_3$O$_4$. Control measurements confirmed the absence of laser-induced changes, indicating that these surface phases pre-exist in the as-deposited film.

However, when measuring TERS under the same aqueous electrochemical conditions used for LiMn$_2$O$_4$, the LiFePO$_4$ vibrational response effectively vanished. The *in situ* TERS spectra were dominated by a broad background (Fig. 4a, blue trace), likely due to fluorescence-like interference or surface reactions at the electrode–electrolyte interface.[51–53] This signal loss is not observed in conventional Raman measurements under identical conditions, as shown in the ESI, section III,† nor in the LiMn$_2$O$_4$ case, and therefore likely reflects a near-surface effect specific to TERS. The origin of the strong fluorescence background observed under *operando* conditions may relate to hydrated or partially delithiated surface species[51–53] and will be the focus of future investigations.

Despite the absence of clear vibrational features, *operando* TERS detected a consistent modulation in the spectral background during redox cycling. By positioning the tip on top of a grain and recording TERS spectra during a CV scan, we observed a reproducible baseline shift correlated with the state-of-charge. Furthermore, a relative intensity TERS map reflecting this background signal matched the topography precisely, clearly identifying the grains as regions of higher intensity (Fig. 4d and g). Although the characteristic LiFePO$_4$ and FePO$_4$ peaks could not be unambiguously identified, the background response reflects surface-level changes synchronized with lithium insertion and extraction. This suggests that TERS remains sensitive to interfacial phenomena even in chemically complex environments and highlights its potential as a diagnostic tool in such systems. Post-cycling *ex situ* TERS confirmed the coexistence of both LiFePO$_4$ and FePO$_4$ phases (ESI, section III†), indicating that redox activity indeed occurred, despite being masked during *operando* measurements. Further
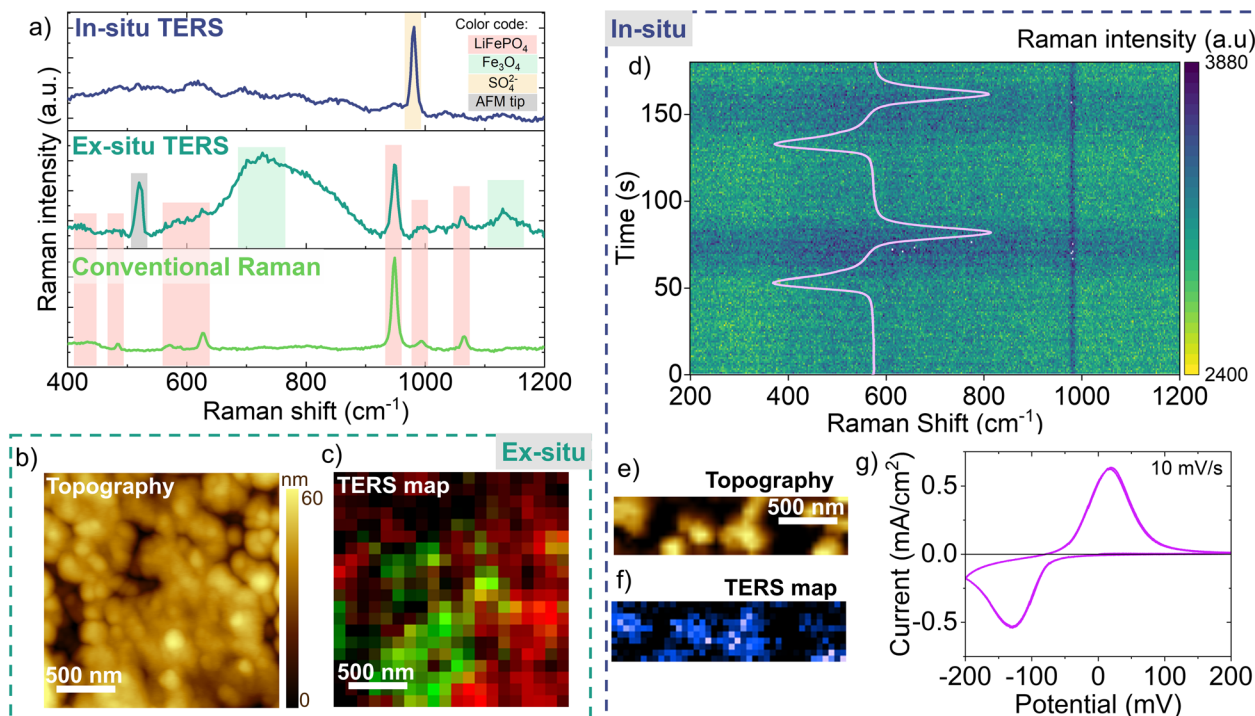
Fig. 4 *Ex situ* and *operando* TERS in LiFePO$_4$. (a) Raman spectra from conventional Raman, *ex situ* TERS (averaged spectra across the map) and *in situ* TERS (averaged spectra across the map in f. (b) *Ex situ* topography and (c) TERS map of the film. With the color code in a, *i.e.*, red LiFePO$_4$ and green Fe$_3$O$_4$. Resolution was set to 100 nm per pixel, acquisition time 2 s per spectra. (d) TERS time map overlaid with the current density with the tip on top of the grain in f. (e) Topography and (f) TERS map plotting the relative intensity changes of the background signal across the map. (g) Cyclic voltammetry for the *operando* TERS.

high-resolution TERS mapping would be needed to elucidate their spatial distribution and structural evolution in more detail.

By capturing distinct interfacial behaviors in two model cathode materials, this work demonstrates the versatility and diagnostic power of *operando* TERS. Even when full spectral resolution is limited, the technique yields valuable insight into local electrochemical dynamics. TERS provides unique perspectives to examine local chemical environments and reaction pathways with nanoscale resolution, which we believe is a critical requirement for advancing solid-state ionics and electrochemistry fields. Conventional Raman Spectroscopy cannot always capture subtle surface or interface phenomena, especially when secondary phases or defect-rich layers are confined to tens of nanometers or even below. In contrast, TERS probes these regions with spatial resolutions matching or even below the characteristic interface dimensions in many battery electrodes and solid electrolytes. This allows direct observation of local lithiation/delithiation, phase transformations, and defect-induced phenomena that would remain hidden when using other measurement techniques.

Besides its spatial resolution, TERS can be coupled with *operando* electrochemical setups, as demonstrated in this work. By correlating time-resolved current–voltage signals with chemical signature changes, TERS allows to visualize *where* and *when* ion transport bottlenecks or accelerations occur,

whether in grains, grain boundaries, or near other functional interfaces (*e.g.*, electrode–electrolyte surfaces). This time-resolved tracking of local phase evolution (including transient or mixed valence states) informs rational design of electrode architectures, doping strategies, and coatings that could enhance overall battery performance. Such *in situ*/*operando* insights could be equally key in understanding ion conduction in solid electrolytes or monitoring degradation in next-generation devices like composite electrodes in all-solid-state batteries. Equally exciting is the potential to extend TERS to systems beyond lithium-ion chemistries, such as sodium-ion, magnesium-ion, or solid oxide fuel cells, where complex reactions at electrode–electrolyte interfaces can limit device reliability. By revealing the interplay between local chemistry, morphological changes and electrochemical performance, TERS can become an essential technique that guides both fundamental materials research and practical energy-storage device engineering.

Conclusions

We have demonstrated the use of *operando* Tip-Enhanced Raman Spectroscopy (TERS) in two model cathode thin films, LiMn$_2$O$_4$ and LiFePO$_4$, aiming to resolve grain- and grain-boundary-specific lithium-ion dynamics. In LiMn$_2$O$_4$, time-

© 2025 The Author(s). Published by the Royal Society of Chemistry

resolved TERS spectra captured phase transitions at the nanoscale, revealing a delayed appearance of the λ-MnO_2 phase at grain boundaries indicative of enhanced Li^+ transport in these regions, as supported by FEM simulations. The results directly link local kinetic asymmetries to structural features, establishing *operando* TERS as a powerful technique for probing interfaces in working battery materials.

By contrast, *operando* TERS on $LiFePO_4$ revealed no resolvable vibrational modes *in situ*, likely due to surface reactivity or amorphization in aqueous electrolyte. Nevertheless, we observed systematic background modulation correlated with the electrochemical cycle, enabling us to correlate Raman signal with electrochemical activity at the nanoscale. Post-cycling *ex situ* TERS confirmed the coexistence of $LiFePO_4$ and $FePO_4$ phases, further proving the sensitivity of the technique.

Our results highlight the nature of grain boundary transport phenomena and the dual advantage of TERS: its ability to spatially resolve functional interfaces and to extract chemically relevant signals even under challenging conditions. By integrating *operando* spectroscopy with electrochemical measurements and numerical modeling, this study opens the door to interrogating ion transport in complex architectures at the nanoscale. *Operando* TERS has the potential to become a useful technique for providing unprecedented insights by mapping dynamic processes at buried interfaces, including space charge layers, interfacial degradation, adsorbates, or proton intercalation, across a wide range of battery chemistries and energy-storage systems.

Methods section

Thin films fabrication. Commercially available ceramic targets of $LiMn_2O_4$ (CODEX) and $LiFePO_4$ (Toshima) were employed for LA PLD (LA-PLD-5000 PVD Products), equipped with a Coherent (Lambda Physik) COMPex Pro 205 KrF excimer laser (λ = 248 nm). These depositions were conducted with a target-substrate distance of 90 mm, constant rotation and laser 1.3 J cm^{-2} laser fluence inside the chamber, at 650 °C and 20 mTorr p_{O2} ($LiMn_2O_4$).[27,38,40,47,54] and at 600 °C and 1 mTorr p_{Ar} ($LiFePO_4$). The substrate was composed of different layers as follows: Pt (70 nm)/Ti (10 nm)/SiO_2 (400 nm) chips of 1 cm^2. The film thickness is 175 nm and 170 nm for $LiMn_2O_4$ and $LiFePO_4$, respectively. XRD measurements were performed to confirm the phase purity for both $LiMn_2O_4$ and $LiFePO_4$ (see ESI, sections I and III,† respectively).

TERS measurements. *Ex situ* and *operando* TERS measurements were carried out using a HORIBA AFM-Raman system, which integrates an OmegaScope AFM with an XploRA Raman spectrometer, along with a potentiostat/galvanostat workstation from Origalys. Our setup is located in a temperature-controlled room with controlled temperature that minimizes thermal and mechanical drift from the AFM stage and the objective scanner. The general protocol to ensure the TERS signal consists of checking the TERS signal on a carbon nanotubes (CNTs) reference sample before and after the experiment. In addition, TERS effect and signal enhancement is demonstrated before and after each map (tip in contact – tip out of contact). Further discussion about the TERS protocol is reported in ESI, section I,† and ref. 28. For the *operando* measurements, we used a custom-designed electrochemical cell provided by Horiba. Our sample was connected as the working electrode (WE), through the Pt border of the chip itself; a Pt counter electrode (CE) was mounted on the left side of the cell, while a metallic cable ran along the border of the cell itself as a pseudo-reference electrode (REF), consisting of an Ag wire. We report a schematic design of the setups in Fig. 1 and further details in the ESI, section I.† The cell is then located inside the AFM sample holder stage. The cell was then filled with 1 M Li_2SO_4 aqueous solution until the window's surface was completely in contact with the liquid. After the probe's location in the cantilever holder, a droplet of water was gently put on the cut lens. This step is necessary to make the first adjustments (*e.g.*, tip feedback laser adjustment) before the tip dips in the cell filled with liquid. The cell cables were connected through a double aperture socket to a potentiostat workstation (Origalys). For TERS measurements a p-polarized 638 nm laser wavelength with a local power of ~3 mW, an Au-coated OMNI TERS tips, a 100× objective for the top view, and a 50× water-immersive objective for the side view were chosen. For AFM, the tapping mode was chosen with an oscillation amplitude of 20 nm. The protocol for the TERS time map acquisition consists of a map of 85 spectra with time acquisition of 1 s per spectra. The CV was performed from 0.5 to 1.05 V with a scan rate of 5 mV s^{-1} for $LiMn_2O_4$ and from −0.2 to 0.2 V with a scan rate of 10 mV s^{-1} for $LiFePO_4$ (according to the aqueous potential window and reference cables). During these holding steps, we acquired a TERS map (total acquisition time 400 s). In all *operando* experiments, the Raman and electrical signals were synchronized by triggering the potentiostat externally with the pulses of the charge-coupled device (CCD) camera of the Raman instruments. Additionally, an oscilloscope was connected to both Raman and potentiostat workstations to visually ensure the synchronism of the signals.

2D finite element modelling. FEM simulations were performed by COMSOL Multiphysics to understand the effect of fast Li diffusivity in grain boundaries. The geometry studied consisted in a 2D out of plane cross-section of the layers, comprising two half grains and one grain boundary, see Fig. 3b. The thickness (170 nm) and lateral size (150 nm) of the grains was directly modeled on our experimental data, while the grain boundary width was fixed to 2 nm. In accordance with previous works,[46,55] the model resolves the Nernst–Planck equations describing insertion and diffusion of Li in the $LiMn_2O_4$ layer. High electronic conductivity of $LiMn_2O_4$ allows to consider a constant electrical potential in the layer[45] and Li transport can be simply simulated by Fick's second law of diffusion:

$$\frac{\partial[\text{Li}]}{\partial t} = -\nabla \cdot (-D_{\text{chem}} \nabla [\text{Li}]) \tag{2}$$

where D_{chem} is the chemical diffusion coefficient. A conventional Butler–Volmer equation was considered for describing

charge transfer and ion insertion at the electrolyte/$LiMn_2O_4$ interface of both grain and grain boundary. Li concentration and cell voltage were related by the equilibrium open circuit voltage profile, derived by Kuwata *et al.*[46] CV simulations were performed varying the electrical potential of the layer at the same rate and with the same limits of the experiments. Diffusivity coefficient of the bulk and charge transfer resistance of the surface are varied until the simulated electrochemical current is comparable to the measured one (see Fig. 3a). In simulated hypothesis 1, the diffusivity of the grain boundary is fixed to be 4 orders of magnitude higher than the bulk. This value is chosen to describe a characteristic case of fast grain boundary diffusivity, not to properly fit the interface diffusivity coefficient. In simulated hypothesis 2, the equilibrium open circuit voltage profile in the grain boundary region is shifted up by 0.3 V, to investigate the effect of a delayed insertion. Finally, in simulated hypothesis 3, two orders of magnitude of decrease of the charge transfer resistance in the grain boundary surface region is set, describing the case of a more facile ion insertion.

Conflicts of interest

The authors declare no conflict of interest.

Data availability

Data for this article, including TERS maps and simulated profiles will be available at IREC's institutional repository, hosted in Zenodo at **https://zenodo.org/communities/irec/**.

Acknowledgements

References

1 M. Lachal, R. Bouchet, A. Boulineau, S. Surblé, C. Rossignol, F. Alloin and S. Obbade, *Solid State Ionics*, 2017, **300**, 187–194.

2 Q. Wang, C. Zhao, X. Hu, J. Wang, S. Ganapathy, S. Eustace, X. Bai, B. Li, H. Li, D. Aurbach and M. Wagemaker, *J. Am. Chem. Soc.*, 2024, **146**(6), 31778–31787.

3 T. Defferriere, D. Klotz, J. C. Gonzalez-Rosillo, J. L. M. Rupp and H. L. Tuller, *Nat. Mater.*, 2022, **21**, 438–444.

4 F. Chiabrera, I. Garbayo, L. López-Conesa, G. Martín, A. Ruiz-Caridad, M. Walls, L. Ruiz-González, A. Kordatos, M. Núñez, A. Morata, S. Estradé, A. Chroneos, F. Peiró and A. Tarancón, *Adv. Mater.*, 2019, **31**, 1805360.

5 A. C. Lazanas and M. I. Prodromidis, *Am. Chem. Soc.*, 2023, **3**(3), 162–193.

6 N. Goswami and R. Kant, *J. Electroanal. Chem.*, 2019, **835**, 227–238.

7 A. L. Lipson, R. S. Ginder and M. C. Hersam, *Adv. Mater.*, 2011, **23**, 5613–5617.

8 A. L. Lipson, K. Puntambekar, D. J. Comstock, X. Meng, M. L. Geier, J. W. Elam and M. C. Hersam, *Chem. Mater.*, 2014, **26**, 935–940.

9 K. L. Anderson and M. A. Edwards, *ACS Meas. Sci. Au*, 2025, **5**(2), 160–177.

10 S. Jesse, A. Kumar, T. M. Arruda, Y. Kim, S. V. Kalinin and F. Ciucci, *MRS Bull.*, 2012, **37**, 651–658.

11 J. Yu, S. Duan, B. Huang, H. Jin, S. Xie and J. Li, *Small Methods*, 2020, **4**(10), 2000308.

12 D. O. Alikin, A. V. Ievlev, S. Y. Luchkin, A. P. Turygin, V. Y. Shur, S. V. Kalinin and A. L. Kholkin, *Appl. Phys. Lett.*, 2016, **108**(11), 113106.

13 J. F. Wu and X. Guo, *Phys. Chem. Chem. Phys.*, 2017, **19**, 5880–5887.

14 A. K. Petford-Long and A. N. Chiaramonti, *Annu. Rev. Mater. Res.*, 2008, **38**, 559–584.

15 L. Yedra, A. Eljarrat, J. M. Rebled, L. López-Conesa, N. Dix, F. Sánchez, S. Estradé and F. Peiró, *Nanoscale*, 2014, **6**, 6646–6650.

16 T. F. Kelly and M. K. Miller, *Rev. Sci. Instrum.*, 2007, **78**(3), 031101.

17 B. Gault, A. Chiaramonti, O. Cojocaru-Mirédin, P. Stender, R. Dubosq, C. Freysoldt, S. K. Makineni, T. Li, M. Moody and J. M. Cairney, *Nat. Rev. Methods Primers*, 2021, **1**, 51.

18 F. Baiutti, F. Chiabrera, D. Diercks, A. Cavallaro, L. Yedra, L. López-Conesa, S. Estradé, F. Peiró, A. Morata,

A. Aguadero and A. Tarancón, *Adv. Mater.*, 2021, **33**(48), 2105622.

19 F. Chiabrera, F. Baiutti, D. Diercks, A. Cavallaro, A. Aguadero, A. Morata and A. Tarancón, *J. Mater. Chem. A*, 2022, **10**, 2228–2234.

20 T. Deckert-Gaudig, A. Taguchi, S. Kawata and V. Deckert, *Chem. Soc. Rev.*, 2017, **46**, 4077–4110.

21 D. Kurouski, M. Mattei and R. P. Van Duyne, *Nano Lett.*, 2015, **15**, 7956–7962.

22 X. Wang, S. C. Huang, T. X. Huang, H. S. Su, J. H. Zhong, Z. C. Zeng, M. H. Li and B. Ren, *Chem. Soc. Rev.*, 2017, **46**, 4020–4041.

23 P. Verma, *Chem. Rev.*, 2017, **117**, 6447–6466.

24 X. Wang, S.-C. Huang, S. Hu, S. Yan and B. Ren, *Nat. Rev. Phys.*, 2020, **2**, 253–271.

25 P. Alonso-González, P. Albella, M. Schnell, J. Chen, F. Huth, A. García-Etxarri, F. Casanova, F. Golmar, L. Arzubiaga, L. E. Hueso, J. Aizpurua and R. Hillenbrand, *Nat. Commun.*, 2012, **3**, 684.

26 B. Pettinger, P. Schambach, C. J. Villagómez and N. Scott, *Annu. Rev. Phys. Chem.*, 2012, **63**, 379–399.

27 J. C. Gonzalez-Rosillo, M. Guc, M. O. Liedke, M. Butterling, A. G. Attallah, E. Hirschmann, A. Wagner, V. Izquierdo-Roca, F. Baiutti, A. Morata and A. Tarancón, *Chem. Mater.*, 2024, **36**, 6144–6153.

28 J. C. Gonzalez-Rosillo, M. Guc, M. O. Liedke, M. Butterling, A. G. Attallah, E. Hirschmann, A. Wagner, V. Izquierdo-Roca, F. Baiutti, A. Morata and A. Tarancón, *Chem. Mater.*, 2024, **36**, 6144–6153.

29 Z. Yang, J. Aizpurua and H. Xu, *J. Raman Spectrosc.*, 2009, **40**, 1343–1348.

30 J. Nanda, G. Yang, T. Hou, D. N. Voylov, X. Li, R. E. Ruther, M. Naguib, K. Persson, G. M. Veith and A. P. Sokolov, *Joule*, 2019, **3**, 2001–2019.

31 G. Yang, X. Li, Y. Cheng, M. Wang, D. Ma, A. P. Sokolov, S. V. Kalinin, G. M. Veith and J. Nanda, *Nat. Commun.*, 2021, **12**, 578.

32 S. Dinda, S. Trivedi, A. Roy, F. D. Pammer and M. Fichtner, *Adv. Energy Mater.*, 2023, **13**(42), 2302176.

33 J. Mürter, S. Nowak, E. Hadjixenophontos, Y. Joshi and G. Schmitz, *Nano Energy*, 2018, **43**, 340–350.

34 C. Schwab, A. Höweling, A. Windmüller, J. Gonzalez-Julian, S. Möller, J. R. Binder, S. Uhlenbruck, O. Guillon and M. Martin, *Phys. Chem. Chem. Phys.*, 2019, **21**, 26066–26076.

35 R. Wang, X. Chen, Z. Huang, J. Yang, F. Liu, M. Chu, T. Liu, C. Wang, W. Zhu, S. Li, S. Li, J. Zheng, J. Chen, L. He, L. Jin, F. Pan and Y. Xiao, *Nat. Commun.*, 2021, **12**, 3085.

36 C. M. Julien and M. Massot, *Raman spectroscopic studies of lithium manganates with spinel structure*, 2003, vol. 15.

37 C. M. Julien, *Solid State Ionics*, 2006, **177**, 11–19.

38 M. Fehse, R. Trócoli, E. Ventosa, E. Hernández, A. Sepúlveda, A. Morata and A. Tarancón, *ACS Appl. Mater. Interfaces*, 2017, **9**, 5295–5301.

39 K. Dokko, Q. Shi, I. C. Stefan and D. A. Scherson, *J. Phys. Chem. B*, 2003, **107**, 12549–12554.

40 V. Siller, J. C. Gonzalez-Rosillo, M. N. Eroles, F. Baiutti, M. O. Liedke, M. Butterling, A. G. Attallah, E. Hirschmann, A. Wagner, A. Morata and A. Tarancón, *ACS Appl. Mater. Interfaces*, 2022, **14**, 33438–33446.

41 N. Kuwata, Y. Matsuda, T. Okawa, G. Hasegawa, O. Kamishima and J. Kawamura, *Solid State Ionics*, 2022, **380**, 115925.

42 J. S. Lee, U. Anselmi-Tamburini, Z. A. Munir and S. Kim, *Electrochem. Solid-State Lett.*, 2006, **9**, J34.

43 N. J. J. De Klerk and M. Wagemaker, *ACS Appl. Energy Mater.*, 2018, **1**, 5609–5618.

44 R. Usiskin and J. Maier, *Adv. Energy Mater.*, 2020, **11**(2), 2001455.

45 A. E. Bumberger, C. Boehme, J. Ring, S. Raznjevic, Z. Zhang, M. Kubicek and J. Fleig, *Chem. Mater.*, 2023, **35**, 5135–5149.

46 N. Kuwata, G. Hasegawa, D. Maeda, N. Ishigaki, T. Miyazaki and J. Kawamura, *J. Phys. Chem. C*, 2020, **124**, 22981–22992.

47 C. Erinmwingbovo, V. Siller, M. Nuñez, R. Trócoli, D. Brogioli, A. Tarancón, A. Morata and F. La Mantia, *ChemElectroChem*, 2023, **202200759**, 1–7.

48 J. Halldin Stenlid, P. Žguns, D. Vivona, A. Aggarwal, K. Gordiz, Y. Zhang, S. Pathak, M. Z. Bazant, Y. Shao-Horn, A. Baskin and J. W. Lawson, *ACS Energy Lett.*, 2024, **9**, 3608–3617.

49 C. Xiao, H. Wang, R. Usiskin, P. A. van Aken and J. Maier, *Science*, 2024, **386**, 407–413.

50 J. Huang, L. Xue, Y. Huang, Y. Jiang, P. Wu, X. Fan and J. Zhu, *Nat. Commun.*, 2024, **15**, 6666.

51 P. He, X. Zhang, Y.-G. Wang, L. Cheng and Y.-Y. Xia, *J. Electrochem. Soc.*, 2008, **155**, A144.

52 I. Bezza, M. Kaus, R. Heinzmann, M. Yavuz, M. Knapp, S. Mangold, S. Doyle, C. P. Grey, H. Ehrenberg, S. Indris and I. Saadoune, *J. Phys. Chem. C*, 2015, **119**, 9016–9024.

53 K. Zaghib, M. Dontigny, P. Charest, J. F. Labrecque, A. Guerfi, M. Kopec, A. Mauger, F. Gendron and C. M. Julien, *J. Power Sources*, 2008, **185**, 698–710.

54 A. Morata, V. Siller, F. Chiabrera, M. Nuñez, R. Trocoli, M. Stchakovsky, A. Tarancón and A. Tarancón, *J. Mater. Chem. A*, 2020, **8**, 11538–11544.

55 F. Brosa Planella, W. Ai, A. M. Boyce, A. Ghosh, I. Korotkin, S. Sahu, V. Sulzer, R. Timms, T. G. Tranter, M. Zyskin, S. J. Cooper, J. S. Edge, J. M. Foster, M. Marinescu, B. Wu and G. Richardson, *Prog. Energy*, 2022, **4**, 042003.